Radiative cooling of solar absorbers using a visibly transparent photonic crystal thermal blackbody

Linxiao Zhu[a,1], Aaswath P. Raman[b,1], and Shanhui Fan[b,2]

[a]Department of Applied Physics, Stanford University, Stanford, CA 94305; and [b]Ginzton Laboratory, Department of Electrical Engineering, Stanford University, Stanford, CA 94305

A solar absorber, under the sun, is heated up by sunlight. In many applications, including solar cells and outdoor structures, the absorption of sunlight is intrinsic for either operational or aesthetic considerations, but the resulting heating is undesirable. Because a solar absorber by necessity faces the sky, it also naturally has radiative access to the coldness of the universe. Therefore, in these applications it would be very attractive to directly use the sky as a heat sink while preserving solar absorption properties. Here we experimentally demonstrate a visibly transparent thermal blackbody, based on a silica photonic crystal. When placed on a silicon absorber under sunlight, such a blackbody preserves or even slightly enhances sunlight absorption, but reduces the temperature of the underlying silicon absorber by as much as 13 °C due to radiative cooling. Our work shows that the concept of radiative cooling can be used in combination with the utilization of sunlight, enabling new technological capabilities.

radiative cooling | thermal radiation | photonic crystal | solar absorber

The universe, at a temperature of 3 K, represents a significant renewable thermodynamic resource: it is the ultimate heat sink. Over midinfrared wavelengths, in particular between 8 and 13 μm, Earth's atmosphere is remarkably transparent to electromagnetic radiation. This wavelength range coincides with the peak wavelength of thermal radiation from terrestrial structures at typical ambient temperatures. Thus, a sky-facing terrestrial object can have radiative access to the universe. Exploiting this radiative access has led to the demonstration of radiative cooling (1–7), as well as proposals for direct electric power generation from thermal radiation of terrestrial objects (8).

Whereas historically radiative cooling was largely developed for night-time applications (1–6, 9–13), recent works have achieved daytime radiative cooling (7, 14). In particular, it was shown that the radiative cooling to below ambient air temperature can be achieved (7), with a photonic structure that reflects almost all incident sunlight and simultaneously emits significant thermal radiation in the midinfrared. Such a structure, being a near-perfect solar reflector, makes no use of incident sunlight. On the other hand, in many applications, including solar cells (15) and outdoor structures (16), the utilization of sunlight through absorption is intrinsic for either operational or aesthetic considerations, but the heating associated with sunlight absorption is undesirable. For these applications, lowering operating temperatures via radiative cooling is only viable if one can simultaneously preserve the absorption of sunlight.

Here we experimentally demonstrate a visibly transparent thermal blackbody, based on a silica photonic crystal, using a thermophotonic approach (17–30). When placed on a silicon absorber under sunlight, such a blackbody preserves and even slightly enhances sunlight absorption, but reduces the temperature of the silicon absorber by as much as 13 °C due to radiative cooling. We also show that for these applications radiative cooling can be combined with convective cooling for enhanced temperature reduction. Our work shows that the concept of radiative cooling can be used in combination with the utilization of sunlight. This opens up new technological possibilities for using the coldness of the

universe to improve the operational performance of a wide range of devices here on Earth.

Results

In our experiment, the solar absorber consists of a 525-μm-thick, 100-mm-diameter double-side–polished crystalline silicon wafer, with a 75-nm-thick silicon nitride antireflection layer on top, and a 200-nm-thick aluminum reflector at the back. To emulate the behavior of a real silicon solar cell, the silicon is p-doped with a resistivity of 1–10 $\Omega \cdot cm$, similar to the base region of a typical crystalline silicon solar cell (31). We will refer to this silicon solar absorber structure as the "bare structure" below.

For the photonic radiative cooling structure we place atop the bare structure, we use silica (SiO_2) as the main constituent material. Silica is transparent over most of the solar wavelength range, while also exhibiting a strong phonon–polariton resonance response in the wavelength range of 8–13 μm that allows it to achieve relatively strong thermal emissivity. We consider two kinds of photonic cooling structures. The first one is a uniform layer of silica that is 500 μm thick. As we discuss later, its properties are suboptimal for radiative cooling, so we seek to improve on its capabilities. Thus, the second structure is a silica photonic crystal layer, fabricated by etching air holes deep into a 500-μm-thick double-side–polished fused silica wafer via photolithography (*Materials and Methods*). The fabricated silica photonic crystal has a square lattice with a periodicity of 6 μm, and with an etching depth of 10 μm, as shown in the scanning electron microscope (SEM) images in Fig. 1 C and D for normal and side views, respectively. The silica photonic crystal is visibly transparent, as shown in Fig. 1E. In the following we will compare the optical and thermal properties of three structures: the bare structure, the

Significance

The coldness of the universe is an enormous but strikingly underexploited thermodynamic resource. Its direct utilization on Earth therefore represents an important frontier for renewable energy research. In many applications, including solar cells and outdoor structures, the absorption of sunlight is intrinsic either from operational or aesthetic considerations, but the resulting heating by sunlight is undesirable. Here we experimentally demonstrate a thermal photonic scheme that can cool these structures by thermal radiation to outer space, while preserving the structures' solar absorption. Our work shows, for the first time to our knowledge, that radiative cooling can be used in combination with the utilization of sunlight, and opens new possibilities for using the coldness of the universe to improve the performance of terrestrial energy systems.
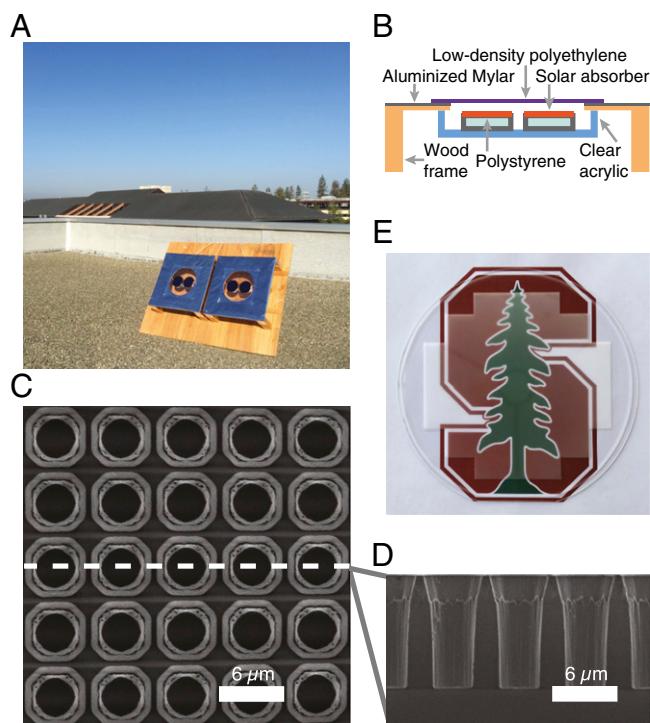
Fig. 1. Rooftop setup and silica photonic crystal. (*A*) Photo of the apparatus and solar absorbers during a test on a rooftop in Stanford, CA. The solar absorbers from left to right are the absorber structure with the planar silica layer, the absorber structure with the silica photonic crystal, and two bare solar absorbers, respectively. (*B*) Cut-out schematic of the apparatus through the middle. Mylar is polyethylene terephthalate. The 12.5-μm-thick polyethylene film used to cover the opening of the chambers is removed for the exposed test. (*C*) Normal-view SEM image of the 2D silica photonic crystal structure that is fabricated and tested in our experiments. It consists of a square-lattice photonic crystal structure with a periodicity of 6 μm made by etching 10-μm-deep air holes into a 500-μm-thick double-side–polished fused silica wafer. (*D*) A side-view SEM image of the photonic crystal structure along the cut denoted by the white dashed line in *C*. (*E*) Photo of the photonic crystal, showing the Stanford logo clearly visible and lying underneath.

uniform silica wafer atop the bare structure, and the silica photonic crystal structure atop the bare structure.

The absorptivity spectra of the three structures over solar wavelengths are experimentally characterized and shown in Fig. 2*A*. The bare structure shows substantial absorption in the wavelength range of 300–1,100 nm, as is typical for a silicon solar absorber (Fig. 2*A*, black curve). The structure achieves near-unity absorption at the wavelength of 600 nm due to the antireflection layer. For the AM1.5 solar spectrum near normal direction, such an absorption spectrum corresponds to an absorbed solar power of 733.2 W/m^2. Placing either of the two photonic cooling structures on top of the bare silicon does not significantly alter the solar absorption properties (Fig. 2*A*, blue and red curves). With a planar silica layer on top of the bare structure, the absorbed solar power is reduced slightly to 724.9 W/m^2. With a silica photonic crystal on top, the absorbed solar power actually increases to 753.2 W/m^2 due to a combination of antireflection and light-trapping effects enabled by the silica photonic crystal.

The emissivity/absorptivity spectra of the three structures over thermal wavelengths are experimentally characterized and shown in Fig. 2*B*. The bare structure has low emissivity at thermal wavelengths (Fig. 2*B*, black curve) and thus should see a relatively small radiative cooling effect when exposed to a clear sky. Adding a planar silica wafer on top of the silicon absorber significantly enhances the emissivity of the structure in the thermal wavelength

range (Fig. 2*B*, blue curve). Nevertheless, the planar structure still exhibits strong emissivity dips around 8–13 μm and 20–30 μm, which are associated with the phonon–polariton resonances of silica. At these wavelengths, silica has a large extinction coefficient (and negative permittivity). Thus, there is strong impedance mismatch between silica and air, leading to large reflectivity, and accordingly small absorptivity and emissivity. The emissivity dip around 8 – 13 μm unfortunately coincides with the atmospheric transparency window, and aligns with the peak blackbody radiation wavelength for typical terrestrial temperatures. Thus, a planar silica layer is suboptimal for radiative cooling. In contrast, placing the silica photonic crystal on top of the silicon absorber results in near-unity emissivity across the thermal wavelength range (Fig. 2*B*, red curve), and such near-unity emissivity persists to large angles (see Fig. 5). Emissivity is higher at all thermal wavelengths and angles relative to that of the structure with the planar silica layer. The use of air holes in the silica photonic crystal, in particular the nonvertical sidewalls of the holes (Fig. 1*D*), results in a gradual refractive index change which provides effective impedance matching between silica and air over a broad range of thermal wavelengths. Taking these measured spectra over solar and thermal wavelength ranges together, we have therefore demonstrated that the silica photonic crystal structure behaves as a visibly transparent thermal blackbody. This spectral behavior is essential for optimally achieving the radiative cooling of solar absorbers that we seek.
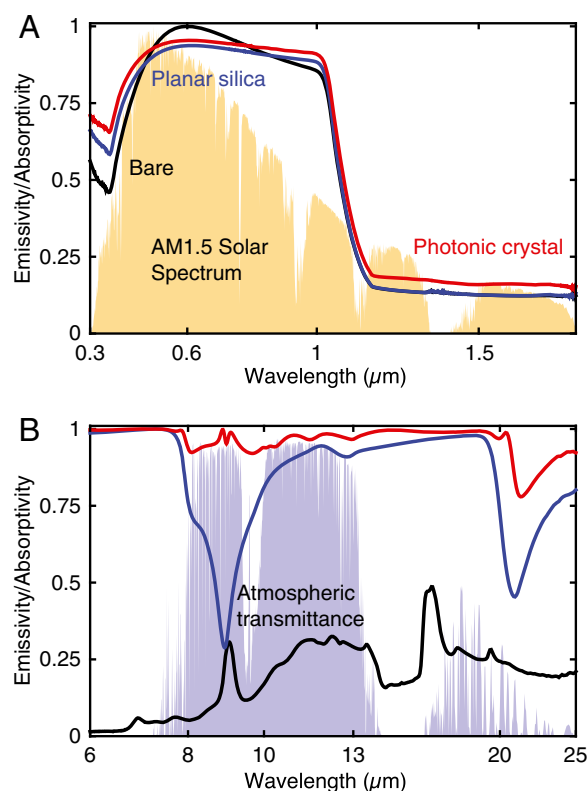
Fig. 2. Emissivity/absorptivity of solar absorbers from the UV to midinfrared. (*A*) Measured emissivity/absorptivity at 8° angle of incidence of solar absorbers over optical and near-infrared wavelengths using an unpolarized light source, with the normalized AM1.5 solar spectrum plotted for reference. (*B*) Measured emissivity/absorptivity of solar absorbers at 10° angle of incidence over midinfrared wavelengths, averaged over both polarizations, with a realistic atmospheric transmittance model for winter in California plotted for ref. 37. In both *A* and *B*, the black, blue, and red curves show the measured emissivity/absorptivity for the bare absorber structure, the absorber structure with the planar silica layer, and the absorber structure with the silica photonic crystal, respectively.
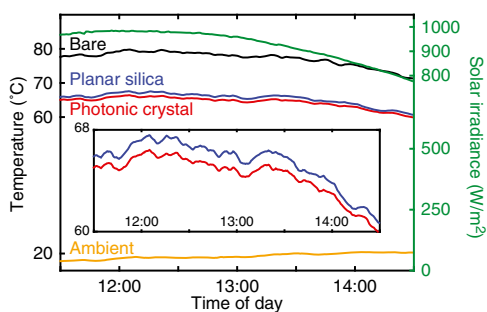
Fig. 3. Steady-state temperature of solar absorbers with a wind shield. Rooftop measurement of the performance of the bare absorber structure (black curve), the absorber structure with the planar silica layer (blue curve), and the absorber structure with the silica photonic crystal (red curve) against ambient air temperature (yellow curve) on a clear winter day with a polyethylene cover in Stanford, CA. The absorber structure with the silica photonic crystal is on average 13 °C cooler than the bare absorber structure, and over 1 °C cooler than the absorber structure with the planar silica layer.

We demonstrate the concept of radiative cooling of solar absorbers by exposing these three characterized structures to the sky on a building roof in Stanford, CA. Testing is done on a clear winter day during daylight hours (Fig. 1*A*). The test setup consists of two chambers placed side by side. The two structures with planar silica layer and with silica photonic crystal layer are placed in the same chamber, to ensure identical environment for these two solar absorbers. Two bare structures are placed in the second chamber so that the overall environments in both chambers are as close as possible. Each chamber consists of acrylic walls, polystyrene supporters for the solar absorbers, and 12.5-μm-thick polyethylene film covering the opening of the chamber that faces the sky, as shown in Fig. 1 *A* and *B*. The polyethylene film is used to reduce the effects from wind while allowing for high transmittance of both solar and thermal radiation. Both chambers are tilted 60° toward the south to maximize solar irradiance on the solar absorbers, such that around noon sunlight is near-normally incident on the solar absorbers with a peak solar irradiance of about 1,000 W/m². The tilting of the samples is a constraint due to testing occurring in winter months when the sun is low in the sky, and in fact reduces sky access for thermal radiation. For the same setup and atmospheric conditions, better cooling performance would be expected if one were to operate the setup without a tilt.

As shown in Fig. 3, the bare solar absorber structure reaches over 50 °C above the ambient air temperature for a 3-h period during which the sky is clear and there is substantial solar irradiance. The absorber structure with planar silica layer is on average around 12 °C cooler than the bare structure, which is directly enabled by the enhanced thermal radiation of the planar silica layer.

Among all three structures tested however, the absorber structure with the photonic crystal layer on top is always the coldest. For the 3 h tested around noon, as shown in Fig. 3, the bare structure with the silica photonic crystal has a temperature that is 13 °C cooler on average compared with the bare structure. Moreover, it is greater than 1 °C cooler than the absorber structure with the planar silica layer. Remarkably, the structure with photonic crystal layer is the coldest, despite the fact that it has the highest solar absorption among all of the structures tested (as inferred from the spectrum measurement shown in Fig. 2). The experimental results here can be well accounted for by a theoretical model that takes into account the electromagnetic response of the absorbers over solar and thermal wavelengths, the thermal leakage effects of the enclosure, the ambient air temperature, and the solar irradiance incident on the structures (see *Materials and Methods* and Fig. 6). The results here highlight that the photonic crystal layer functions as a visibly transparent thermal blackbody that

maintains the underlying solar absorber cooler by emitting thermal radiation nearly optimally, in particular, to the cold of outer space.

For an object above ambient air temperature, one can combine radiative cooling with nonradiative cooling mechanisms for enhanced temperature reduction. We demonstrate this combined cooling process by removing the polyethylene cover and exposing the three structures to the sky on another winter day with similar conditions. As shown in Fig. 4, all three structures are significantly cooler than the covered counterparts in Fig. 3, as they have access to substantial convective and forced air cooling by strong winds present during that day. Nevertheless, the absorber structure with photonic crystal layer on top is still the coldest, even though it causes enhanced solar absorption into the silicon solar absorber. For the 3 h tested around noon shown in Fig. 4, the absorber structure with photonic crystal is on average 5.2 °C cooler than the bare structure, and 1.3 °C cooler than the absorber structure with the planar silica layer. The experimental results here can be well accounted for by the same theoretical model used previously and additionally accounting for the effect of convective and forced air cooling given the ambient temperature and the wind speed during the day testing occurred (see *Materials and Methods* and Fig. 7). The results here show that radiative cooling can in fact be used in combination with convective and forced air cooling. Indeed, the effect of radiative cooling can be prominent even in the presence of other significant cooling mechanisms.

Discussion

We have experimentally demonstrated a thermophotonic approach to substantial, passive, radiative cooling of a solar absorber, by radiating heat to the cold of outer space through the atmosphere's infrared transparency window. By placing a silica photonic crystal on top of a silicon substrate, we lower the temperature of the substrate by as much as 13 °C, while maintaining and even slightly enhancing solar absorption. Here the silica photonic crystal functions as a visibly transparent thermal blackbody, which is key to achieving optimal radiative cooling for solar absorbers, and will likely be an important tool more generally for advanced thermal management.

The measured temperature reduction with the silica photonic crystal structure is constrained by the fact that the silica photonic crystal enhances sunlight absorption in the absorber structure. Provided the same solar absorption power for the solar absorbers, the absorber structure with the silica photonic crystal would show a much larger temperature reduction, compared with the absorber
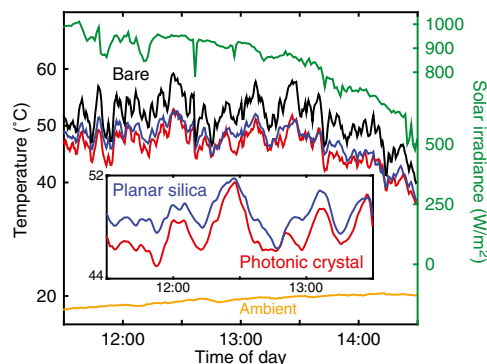
Fig. 4. Steady-state temperature of solar absorbers without a wind shield. Rooftop measurement of the performance of the bare absorber structure (black curve), the absorber structure with the planar silica layer (blue curve), and the absorber structure with the silica photonic crystal (red curve) against ambient air temperature (yellow curve) on a clear winter day without a polyethylene cover in Stanford, CA. The absorber structure with the silica photonic crystal is on average 5.2 °C cooler than the bare absorber structure, and over 1.3 °C cooler than the absorber structure with the planar silica layer. (*Inset*) A running average of the temperature data over an averaging period of 8 min.
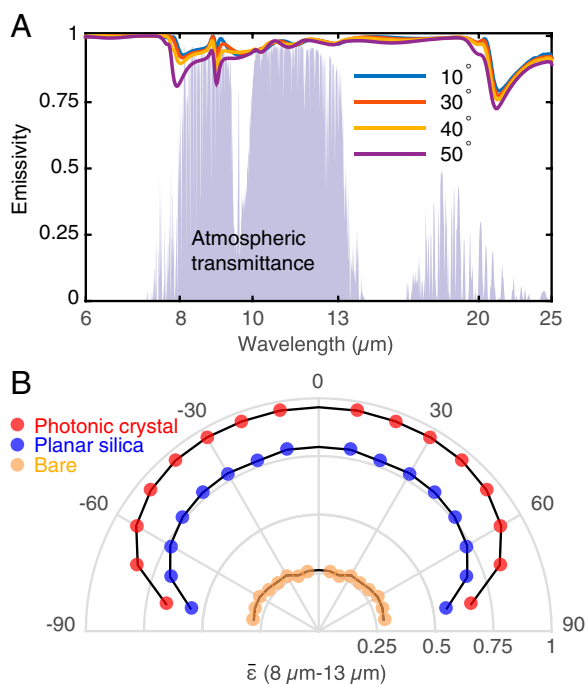
Fig. 5. Angular emissivity of solar absorbers. (*A*) Measured emissivity of the absorber structure with the silica photonic crystal at variable angles of incidence, over midinfrared wavelengths, averaged over both polarizations, with a realistic atmospheric transmittance model for winter in California plotted for ref. 37. (*B*) Average measured emissivity $\bar{\varepsilon}$ of the solar absorbers between 8 and 13 μm (the atmospheric transparency window) plotted as a function of polar angle of incidence. The yellow, blue, and red circles show the average emissivity for the bare absorber structure, the absorber structure with the planar silica layer, and the absorber structure with the silica photonic crystal, respectively. The emissivity for the absorber structure with the silica photonic crystal remains near-unity between 10° and 50° (96.2% at 10°, and 94.1% at 50°), and remains high even at larger angles of incidence. At all angles of incidence, the absorber structure with the silica photonic crystal shows a substantially higher emissivity than the bare structure and the absorber structure with the planar silica layer.

structure with the planar silica layer (*Materials and Methods*). Our results here also point to the intriguing possibility of designing the top layers to simultaneously enhance solar absorption while cooling the solar cell. Also, the cooling performance achieved here is constrained by the tilt needed to conduct testing under direct sunlight during winter months. For the same setup and atmospheric conditions, better cooling performance would be expected if one were to operate the setup without a tilt.

Our experiments point to a universal approach for cooling outdoor structures and devices that require significant solar absorption for functional or aesthetic purposes. One potential important application is to cool solar cells. Every 1 °C increase in the solar cell's operating temperature leads to a relative efficiency decline of about 0.45% (32) for crystalline silicon. Thus, for a crystalline silicon solar cell with efficiency around 20 % (33), the 13 °C temperature reduction demonstrated here would translate to an absolute efficiency improvement of over one percentage point, which would be a very substantial improvement for solar cell efficiency. Practical solar cells have encapsulation layers made of polymer and silica. These layers do have strong thermal emissivity and hence can potentially have a cooling effect. However, the thermal emissivity of these layers is typically not optimized. Moreover, to achieve the cooling of the solar cell layer beneath such encapsulation layers, efficient heat conduction between the top of the encapsulation layers and the solar cell layer will be essential. Previous simulations have indicated that reducing the silica layer thickness is beneficial if the

silica layer is to be used for radiative cooling purposes (15). Our experimental work here points to the importance of considering the thermal emission properties of layers atop the silicon absorber layer in the overall design and optimization of encapsulated solar cells. This strategy may also be important for automobile applications where the need for air-conditioning can reduce fuel economy by 20% (34).

We have used photolithography and etching to fabricate a silica photonic crystal at wafer scale. Alternatively, photolithography-free patterning methods, such as nanoimprint (35), and Langmuir–Blodgett assembly and etching (36), may be used to fabricate silica photonic crystals and microstructures in general at lower cost and larger scales. Moreover, although we have realized a visibly transparent thermal blackbody with the use of a silica photonic crystal, there are likely other approaches to achieving the same functionality, including multilayer dielectric coatings, that are even more cost-effective for large-scale fabrication. Finally, previous work on radiative cooling under the sun uses near-perfect solar reflector, which makes no use of sunlight. Our results however show that radiative cooling can be used both independently and in conjunction with other conventional cooling mechanisms, to passively maintain lower temperatures with the utilization of sunlight. This opens up new possibilities for exploiting the cold of outer space to improve the efficiency of terrestrial energy systems in general.

Materials and Methods

Fabrication of Solar Absorbers. The fabrication of the bare solar absorber started with a 525-μm-thick, 100-mm-diameter, p-doped double-side–polished crystalline silicon wafer, with resistivity 1–10 Ω·cm, from Nova Electronic Materials. A 200-nm-thick layer of aluminum was first evaporated on one side of the silicon wafer using electron beam evaporation, followed by a 75-nm-thick layer of silicon nitride deposited on the other side of the silicon wafer using plasma-enhanced chemical vapor deposition.

The absorber structure with the planar silica layer was constructed by placing a 500-μm-thick, 100-mm-diameter double-side–polished fused silica wafer atop the bare solar absorber. A thin layer of refractive index matching liquid (Cargille Laboratories) was applied between the top fused silica and the bare absorber structure, to match the refractive index of fused silica over the solar wavelength range, and to prevent the formation of any air layer between the top fused silica and the bottom structure. The index matching liquid is transparent and does not absorb sunlight by itself.

The absorber structure with silica photonic crystal was constructed by placing a silica photonic crystal on top of a bare solar absorber, with the index matching liquid applied in between. The fused silica photonic crystal was fabricated using photolithography at the Stanford Nanofabrication Facility. The patterning was first etched onto a chrome photomask (Compugraphics). A 7-μm-thick SPR 220–7.0 positive photoresist was spun on one side of a 500-μm-thick, 100-mm-diameter double-side–polished fused silica wafer. The photoresist-covered fused silica wafer was exposed under the chrome photomask in a mask aligner (Karl Suss MA-6). After developing, the wafer with the patterned photoresist was dry etched to 10-μm depth using CHF_3–O_2 chemistry with inductively coupled plasma reactive-ion etching (Plasma-Therm Versaline ICP). Remaining photoresist and residues were stripped off by plasma ashing.

Characterization of Solar Absorbers. The reflectance of the solar absorbers was characterized in the visible and near-infrared using a spectrophotometer (Agilent Cary 6000i) with an unpolarized light source and a high Lambertian reflectance standard (Labsphere SRS-99-020), and is shown in Fig. 2*A*. A diffuse reflectance accessory (DRA 1800) with a 150-mm-diameter integrating sphere was used to collect both specular and diffuse components of reflection at 8° angle of incidence. In the infrared, a Fourier transform infrared spectrometer (Thermo Scientific Nicolet 6700) was used to characterize the reflectance of the solar absorbers with a gold film used as a reflectance standard, as shown in Fig. 2*B*. A variable-angle reflection accessory (Harrick Seagull) equipped with a KRS-5 substrate-based wire grid polarizer (Harrick) allows for reflectance measurements at varying angles of incidence for both polarizations (see Fig. 5 for data). An SEM (FEI NovaSEM 450) was used to image the silica photonic crystal at both normal and side views in Fig. 1 *C* and *D*.

Rooftop Measurement. The solar absorbers were tested on a flat building roof (Fig. 1*A*) in Stanford, CA, in mid-November 2014. The sun's peak elevation was around 30° above the horizon on the days testing occurred, whereas the
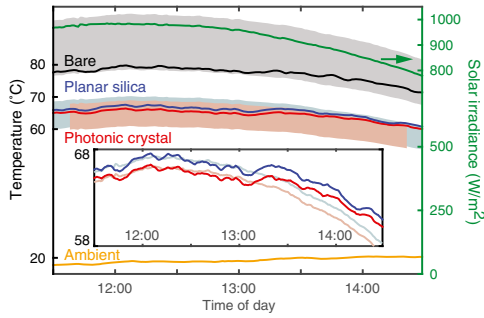
Fig. 6. Modeling of steady-state temperature of solar absorbers with a wind shield. The modeled steady-state temperatures for the bare solar absorber, the absorber structure with the planar silica layer, and the absorber structure with the silica photonic crystal are shown as the gray, light blue, and light red bands, respectively, for an h_c value range from 6.5 to 9.1 $Wm^{-2} \cdot K^{-1}$. The experimentally observed values for the temperatures of the bare solar absorber, the absorber structure with the planar silica layer, and the absorber structure with the silica photonic crystal are shown by the black, blue, and red curves, respectively, with the ambient air temperature as the yellow curve. The solar irradiance measured in the same course of time is shown as the green curve. The experimental observations match quite well with the modeling. (*Inset*) Zoomed-in view of the experimentally measured steady-state temperatures of the absorber structures with the planar silica layer and silica photonic crystal, compared with modeling using a combined nonradiative heat exchange coefficient h_c as 7.3 $Wm^{-2} \cdot K^{-1}$, showing excellent agreement between modeling and experiments. In this case, we use a thin polyethylene film to cover the opening of the chamber to reduce effects from winds.

apparatus containing the solar absorbers was placed on a platform tilted 60° toward the south. Thus, at maximum solar irradiance sunlight is near-normally incident on the absorber structures.

The apparatuses containing the solar absorbers consist of a wood frame covered by a layer of aluminized Mylar. A clear acrylic box with the top side open is joined and sealed to the underside of the wooden frame's top surface. An aluminized Mylar-coated polystyrene pedestal is glued on the acrylic box. In the experiment with the wind shield (Fig. 3), a 12.5-μm-thick, low-density polyethylene film is used to cover the top aperture of the wooden frame, and serves as an infrared-transparent cover. This design, schematically represented in Fig. 1B, creates a stable environment for testing. In another experiment without the wind shield (Fig. 4), the top aperture of the wooden frame is left open to test the performance of radiative cooling in the presence of strong convective and forced-air cooling.

The back surfaces of the solar absorbers are instrumented with an adhesive resistance temperature detector sensor with ±0.15 °C accuracy mounted on the center of the structures, connected to a data logger (Omega OM-CP-OCTRTD). To accurately compare the performance, an absorber structure with the planar silica layer and an absorber structure with the silica photonic crystal were positioned inside the same chamber, to ensure identical environment for these two absorber structures. Two bare solar absorber structures were positioned in the same chamber so that the environment in the second chamber is as close to the first chamber as possible. The solar absorbers were exposed to the clear sky under direct sunlight. Solar irradiance incident on the solar absorbers is measured over the same time period using a pyranometer (Kipp & Zonen CMP 6) and a data logger rated to a directional error of ±20 W/m². The pyranometer was placed on the same tilted platform as the apparatuses. Ambient air temperature is measured using an air-temperature resistance temperature detector probe with ±0.15 °C accuracy behind the platform, with free airflow and without access to direct sunlight irradiance.

Modeling Steady-State Temperatures of Solar Absorbers. Consider a solar absorber at temperature T, with spectral angular emissivity $\varepsilon(\lambda, \Omega)$. When the solar absorber is exposed to a clear daylight sky, it is subject to both solar irradiance, and thermal radiation from the atmosphere (corresponding to ambient air temperature T_{amb}). The steady-state temperature T of the solar absorber is determined by

$$P_{rad}(T) - P_{atm}(T_{amb}) - P_{sun} + P_{cond+conv} = 0. \quad [1]$$

In Eq. **1**, the thermal emission power radiated out by the solar absorber is

$$P_{rad}(T) = \int d\Omega cos\theta \int_0^\infty d\lambda I_{BB}(T, \lambda)\varepsilon(\lambda, \Omega). \quad [2]$$

Here, $\int d\Omega = \int_0^{\pi/2} d\theta sin\theta \int_0^{2\pi} d\phi$ is the angular integral over a hemisphere, $I_{BB}(T, \lambda) = (2hc^2/\lambda^5)/[e^{hc/(\lambda k_B T)} - 1]$ is the spectral radiance of a blackbody at temperature T, where h is the Planck constant, c is the velocity of light, k_B is the Boltzmann constant, and λ is wavelength.

$$P_{atm}(T_{amb}) = \int d\Omega cos\theta \int_0^\infty d\lambda I_{BB}(T_{amb}, \lambda)\varepsilon(\lambda, \Omega)\varepsilon_{atm}(\lambda, \Omega), \quad [3]$$

is the absorbed thermal radiation from the atmosphere.

$$P_{sun} = \int_0^\infty d\lambda\varepsilon(\lambda, \theta_{sun})I_{AM1.5}(\lambda)\cos(\theta_{sun}), \quad [4]$$

is solar absorption power. In Eqs. **3** and **4**, we have used Kirchhoff's law to replace absorptivity with emissivity $\varepsilon(\lambda, \Omega)$. The angle-dependent emissivity of the atmosphere is given by ref. 3: $\varepsilon_{atm}(\lambda, \Omega) = 1 - t(\lambda)^{1/cos\theta}$, where $t(\lambda)$ is the atmospheric transmittance in the zenith direction. The solar irradiance is represented by the AM1.5 spectrum. The P_{sun} is devoid of an angular integral, and the structure's emissivity is represented by its value at incidence angle θ_{sun}.

$$P_{cond+conv} = h_c(T - T_{amb}), \quad [5]$$

is heat loss due to nonradiative heat exchange. Here h_c is the combined nonradiative heat coefficient taking into account both the conductive and convective processes due to the contact of the solar absorber with external surfaces and the air adjacent to the solar absorber.

We model steady-state temperatures of the solar absorbers using Eq. **1**, and compare them to the experimental data of the solar absorber temperatures. Specifically, we input the experimentally derived absorption/emission data of the solar absorbers for the relevant angles of incidence, the AM1.5 spectrum weighed to the measured solar irradiance, and a model of atmosphere transmittance. MODTRAN5 is used to model the atmosphere in the infrared for a clear sky at midlatitude during the winter (37). The model accounts for the tilt of the apparatus. For the case with polyethylene cover (Fig. 3), the model accounts for the presence of the thin polyethylene film.
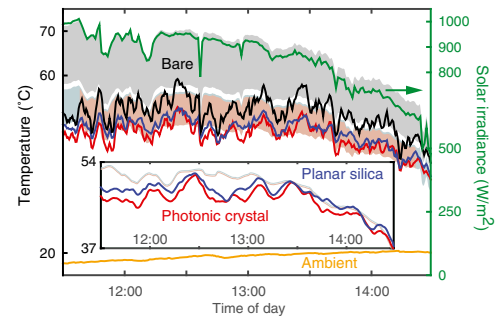
Fig. 7. Modeling of steady-state temperature of solar absorbers without a wind shield. The modeled steady-state temperatures for the bare solar absorber, the absorber structure with the planar silica layer, and the absorber structure with the silica photonic crystal are shown as the gray, light blue, and light red bands, respectively, for an h_c value range from 11.6 to 16 $Wm^{-2} \cdot K^{-1}$. The experimentally observed values for the temperatures of the bare solar absorber, the absorber structure with the planar silica layer, and the absorber structure with the silica photonic crystal are shown by the black, blue, and red curves, respectively, with the ambient air temperature as the yellow curve. The solar irradiance measured in the same course of time is shown as the green curve. The experimental observations match quite well with the modeling. (*Inset*) Zoomed-in view of the experimentally measured steady-state temperatures of the absorber structures with the planar silica layer and silica photonic crystal, compared with modeling using a combined nonradiative heat exchange coefficient h_c as 13.6 $Wm^{-2} \cdot K^{-1}$, showing reasonably good agreement between modeling and experiments. The measured temperatures in the inset are with running average over an averaging period of 8 min. In this case, the absorbers are subject to effects of winds.

Zhu et al.

Given the observed ambient air temperatures and measured solar irradiance, in addition to the measured spectral angular emissivity of the solar absorbers (measured from 10° to 80°) and the atmospheric transmission from MODTRAN5, we solve Eq. **1** for steady-state temperature, and plot the result as the shaded bands in Fig. 6. The modeling results for the bare absorber structure, the absorber structure with the planar silica layer, and the absorber structure with the silica photonic crystal, are shown by the gray, light blue, and light red bands, respectively. The bounds of the bands are defined by a range of combined nonradiative heat exchange coefficient h_c between 6.5 and 9.1 $Wm^{-2} \cdot K^{-1}$, because h_c can vary over the course of a day given varying environmental conditions. The model matches the observed temperatures of the solar absorbers quite well. In Fig. 6 (*Inset*), we show a blown-up plot of the predicted temperature for the absorber structure with silica photonic crystal (light red curve) and the absorber structure with planar silica layer (light blue curve), compared with the experimentally observed values, using h_c as 7.3 $Wm^{-2} \cdot K^{-1}$. This value of h_c is consistent with the nonradiative exchange coefficient for a similar chamber in ref. 7. We observe that the model predicts values very close to the experimentally observed values, and the temperature reduction of the absorber with silica photonic crystal compared with the absorber with the planar silica layer matches the experimental counterpart quite well, with 1.03 °C modeled compared with 1.0 °C in the experiment.

For testing without the wind shield, we perform similar modeling of the steady-state temperatures of the solar absorbers, as shown in Fig. 7, where we have plotted bands by varying h_c from 11.6 to 16 $Wm^{-2} \cdot K^{-1}$. The wind speed reported by local weather stations during the time of the experiment is 2.6 m/s. The nonradiative heat exchange coefficient between the top surface and air corresponding to this wind speed is 10.6 $Wm^{-2} \cdot K^{-1}$ (6), which agrees well with the combined nonradiative heat exchange coefficient values we use. From modeling, we observe that the absorber structure with silica photonic crystal is

generally predicted to be slightly cooler than the absorber structure with planar silica layer, agreeing with the experimental data. For h_c as 13.6 $Wm^{-2} \cdot K^{-1}$, as shown in Fig. 7 (*Inset*), the absorber structure with silica photonic crystal is modeled to be on average 0.27 °C cooler than the absorber structure with the planar silica layer, which compares reasonably well with the experimentally measured temperature reduction, considering that the solar absorbers were subject to direct wind influences.

We note that the measured temperature reduction of the absorber with the silica photonic crystal, compared with the absorber with the planar silica layer, is affected by the enhanced solar absorption enabled by the silica photonic crystal. To highlight the cooling performance purely from enhanced thermal radiation, we perform a modeling study where we assume that the absorber with silica photonic crystal absorbs the same amount of sunlight as the absorber with the planar silica layer. The modeling takes into account measured ambient temperature and solar irradiance, from the experiment with wind shield in Fig. 3, and a combined nonradiative heat exchange coefficient h_c as 7.3 $Wm^{-2} \cdot K^{-1}$ as used in the modeling of Fig. 6. The modeling shows that, with the same amount of sunlight absorption, the absorber structure with the silica photonic crystal would be on average 2.79 °C cooler than the absorber with the planar silica layer, in contrast with the observed 1.03 °C difference in Fig. 6.

1. Trombe F (1967) Perspectives sur l'utilisation des rayonnements solaires et terrestres dans certaines régions du monde. *Revue Generale de Thermique* 6(70):1285.
2. Catalanotti S, et al. (1975) The radiative cooling of selective surfaces. *Sol Energy* 17(2):83–89.
3. Granqvist CG, Hjortsberg A (1981) Radiative cooling to low temperatures: General considerations and application to selectively emitting SiO films. *J Appl Phys* 52(6):4205.
4. Berdahl P (1984) Radiative cooling with MgO and/or LiF layers. *Appl Opt* 23(3):370–372.
5. Orel B, Gunde M, Krainer A (1993) Radiative cooling efficiency of white pigmented paints. *Sol Energy* 50(6):477–482.
6. Nilsson TM, Niklasson GA (1995) Radiative cooling during the day: simulations and experiments on pigmented polyethylene cover foils. *Sol Energy Mater Sol Cells* 37(1):93–118.
7. Raman AP, Anoma MA, Zhu L, Rephaeli E, Fan S (2014) Passive radiative cooling below ambient air temperature under direct sunlight. *Nature* 515(7528):540–544.
8. Byrnes SJ, Blanchard R, Capasso F (2014) Harvesting renewable energy from Earth's mid-infrared emissions. *Proc Natl Acad Sci USA* 111(11):3927–3932.
9. Granqvist CG, Hjortsberg A (1980) Surfaces for radiative cooling: Silicon monoxide films on aluminum. *Appl Phys Lett* 36(2):139.
10. Berdahl P, Fromberg R (1982) The thermal radiance of clear skies. *Sol Energy* 29(4):299–314.
11. Berdahl P, Martin M, Sakkal F (1983) Thermal performance of radiative cooling panels. *Int J Heat Mass Transfer* 26(6):871–880.
12. Smith G (2009) Amplified radiative cooling via optimised combinations of aperture geometry and spectral emittance profiles of surfaces and the atmosphere. *Sol Energy Mater Sol Cells* 93(9):1696–1701.
13. Gentle AR, Smith GB (2010) Radiative heat pumping from the Earth using surface phonon resonant nanoparticles. *Nano Lett* 10(2):373–379.
14. Rephaeli E, Raman A, Fan S (2013) Ultrabroadband photonic structures to achieve high-performance daytime radiative cooling. *Nano Lett* 13(4):1457–1461.
15. Zhu L, Raman A, Wang KX, Anoma MA, Fan S (2014) Radiative cooling of solar cells. *Optica* 1(1):32–38.
16. Zhu L, Raman A, Fan S (2013) Color-preserving daytime radiative cooling. *Appl Phys Lett* 103(22):223902.
17. Lin SY, et al. (2000) Enhancement and suppression of thermal emission by a three-dimensional photonic crystal. *Phys Rev B* 62(4):R2243–R2246.
18. Greffet JJ, et al. (2002) Coherent emission of light by thermal sources. *Nature* 416(6876):61–64.
19. Luo C, Narayanaswamy A, Chen G, Joannopoulos JD (2004) Thermal radiation from photonic crystals: A direct calculation. *Phys Rev Lett* 93(21):213905.
20. Narayanaswamy A, Chen G (2004) Thermal emission control with one-dimensional metallodielectric photonic crystals. *Phys Rev B* 70(12):125101.
21. Lee BJ, Fu CJ, Zhang ZM (2005) Coherent thermal emission from one-dimensional photonic crystals. *Appl Phys Lett* 87(7):071904.
22. Schuller JA, Taubner T, Brongersma ML (2009) Optical antenna thermal emitters. *Nat Photonics* 3(11):658–661.
23. Liu X, et al. (2011) Taming the blackbody with infrared metamaterials as selective thermal emitters. *Phys Rev Lett* 107(4):045901.
24. Zoysa MD, et al. (2012) Conversion of broadband to narrowband thermal emission through energy recycling. *Nat Photonics* 6(8):535–539.
25. Yeng YX, et al. (2012) Enabling high-temperature nanophotonics for energy applications. *Proc Natl Acad Sci USA* 109(7):2280–2285.
26. Wu C, et al. (2012) Metamaterial-based integrated plasmonic absorber/emitter for solar thermo-photovoltaic systems. *J Opt* 14(2):024005.
27. Arpin KA, et al. (2013) Three-dimensional self-assembled photonic crystals with high temperature stability for thermal emission modification. *Nat Commun* 4:2630.
28. Molesky S, Dewalt CJ, Jacob Z (2013) High temperature epsilon-near-zero and epsilon-near-pole metamaterial emitters for thermophotovoltaics. *Opt Express* 21(S1):A96–A110.
29. Lenert A, et al. (2014) A nanophotonic solar thermophotovoltaic device. *Nat Nanotechnol* 9(2):126–130.
30. Inoue T, De Zoysa M, Asano T, Noda S (2014) Realization of dynamic thermal emission control. *Nat Mater* 13(10):928–931.
31. Goetzberger A, Knobloch J, Voss B (1998) *Crystalline Silicon Solar Cells* (Wiley, New York), p 123.
32. Skoplaki E, Palyvos J (2009) On the temperature dependence of photovoltaic module electrical performance: A review of efficiency/power correlations. *Sol Energy* 83(5):614–624.
33. Saga T (2010) Advances in crystalline silicon solar cell technology for industrial mass production. *NPG Asia Materials* 2(3):96–102.
34. Farrington R, Rugh J (2000) Impact of Vehicle Air-Conditioning on Fuel Economy, Tailpipe Emissions, and Electric Vehicle Range. *NREL/CP-540-28960*. Available at www.nrel.gov/docs/fy00osti/28960.pdf. Accessed March 3, 2015.
35. Peroz C, Chauveau V, Barthel E, Søndergård E (2009) Nanoimprint lithography on silica sol-gels: A simple route to sequential patterning. *Adv Mater* 21(5):555–558.
36. Hsu CM, Connor ST, Tang MX, Cui Y (2008) Wafer-scale silicon nanopillars and nanocones by Langmuir-Blodgett assembly and etching. *Appl Phys Lett* 93(13):133109.
37. Berk A, et al. (2006) MODTRAN5: 2006 update. *Proc SPIE* 6233:62331F.